Abnormal Assemblies and Subunit Exchange of αB-Crystallin R120 Mutants Could Be Associated with Destabilization of the Dimeric Substructure[†]

Magalie Michiel,[‡] Fériel Skouri-Panet,[§] Elodie Duprat,[‡] Stéphanie Simon,[||] Céline Férard,[§] Annette Tardieu,[‡] and Stéphanie Finet*[,‡]

PBSF, CNRS-UPMC, case 29, 7 quai St. Bernard, 75252 Paris CEDEX 5, France, IMPMC, CNRS-IPGP-UPMC-Université Paris Diderot, 140 rue de Lourmel 75015 Paris, France, and CGMC, UMR5534, CNRS-Université Lyon 1, Bâtiment G. Mendel, 43 Bd du 11 Novembre 1918, 69622 Villeurbanne CEDEX, France

Received August 8, 2008; Revised Manuscript Received September 19, 2008

ABSTRACT: Mutation of the Arg120 residue in the human αB-crystallin sequence has been shown to be associated with a significant ability to aggregate in cultured cells and have an increased oligomeric size coupled to a partial loss of the chaperone-like activity *in vitro*. In the present study, static and dynamic light scattering, small-angle X-ray scattering, and size exclusion chromatography were used to follow the temperature and pressure induced structural transitions of human αB-crystallin and its R120G, R120D, and R120K mutants. The wild type αB-crystallin was known to progressively increase in size with increasing temperature, from 43 to 60 °C, before aggregating after 60 °C. The capacity to increase in size with temperature or pressure, while remaining soluble, had disappeared with the R120G mutant and was found to be reduced for the R120K and R120D mutants. The R120K mutant, which preserves the particle charge, was the less impaired. The deficit of quaternary structure plasticity was well correlated with the decrease in chaperone-like activity previously observed. However, the mutant ability to exchange subunits, measured with a novel anion exchange chromatography assay, was found to be increased, suggesting subtle relationships between structural dynamics and function. From molecular dynamic simulations, the R120 position appeared critical to conserve proper intra- and intersubunit interactions. *In silico* mutagenesis followed by simulated annealing of the known small heat shock protein 3D structures suggested a destabilization of the dimeric substructure by the R120 mutations. The whole of the results demonstrated the importance of the R120 residue for structural integrity, both static and dynamic, in relation with function.

The αB-crystallin (αB)[1] belongs to the small heat shock protein (sHSP) family. The sHSPs are ubiquitous proteins, usually expressed to protect cells against a variety of stress (*1, 2*). In humans, 11 sHSPs are known (ref *3* and references therein, *4*), including αA-crystallin (hαA), which is essentially expressed in the lens, and hαB, which is also expressed in other tissues such as muscles. In lenses, αA and αB, only found mixed in variable ratios, formed the so-called αN for native α-crystallins. An increasing number of point mutations leading to pathologies have now been identified. The most well known is the mutation of Arg-120 to Gly in hαB (R120G), which is responsible for an autosomal dominant desmin-related myopathy associated with cardiomyopathy and cataract (*5*). The corresponding mutations in hαA (R116C) and HSP22 (K141E or K141N) are also involved in inherited human diseases (*6, 7*), and several mutations in HSP27, located in the vicinity of the residue at the equivalent 120 position, (R127W, S135F, R136W, R140G, K141Q) are implicated in axonal Charcot−Marie–Tooth disease and distal hereditary motor neuropathy (*8, 9*).

The sHSP family is characterized by a highly conserved C-terminal domain, the α-crystallin domain (ACD) (*10*), and the variable N-terminal domain and C-terminal extension. A typical feature of sHSPs is the formation of large assemblies, either monodisperse or polydisperse (2−40 subunits of 12−50 kDa). The origin of such a diversity remains unknown at present. Moreover, within each sHSP class, the number of subunits is further controlled by the environmental conditions, through subunit exchange. So far, only three three-dimensional (3D) structures of sHSPs are known, one from a hyperthermophile archae *Methanoccus jannaschii*, HSP16.5, with 24 subunits (*11*); one from wheat, *Triticum aestivum*, HSP16.9, with 12 subunits (*12*); and one from a parasitic flatworm, *Taenia saginata*, Tsp36, with 2

[†] This work was supported by the French Ministry of Research (to M.M.), by the Association Française contre les Myopathies (AFM) (to S.S. and Grant 12594)), by the University Pierre et Marie Curie, UPMC (to F.S.-P., C.F., A.T., and S.F.), and by the Centre National de la Recherche Scientifique, CNRS (to F.S.-P., C.F., A.T., and S.F.).

* To whom correspondence should be addressed. Phone: 33144273685. Fax: 33144273699. E-mail: stephanie.finet@upmc.fr.

[‡] PBSF, CNRS-UPMC.

[§] IMPMC, CNRS-IPGP-UPMC-Université Paris Diderot.

[||] CGMC, UMR5534, CNRS-Université Lyon 1.

[1] Abbreviations. αA, αA-crystallin; αB, αB-crystallin; bαN, bovine αN-crystallin; hαB-WT, human αB-crystallin wild-type; sHSPs, small heat shock proteins; ACD, α-crystallin domain; 3D, three-dimensional; IPTG, isopropyl α-D-thiogalactoside; PMSF, phenyl-methyl-sulfonyl fluoride; DLS, dynamic light scattering; R_h, hydrodynamic radius; Pd, polydispersity; SAXS, small-angle X-ray scattering; R_g, radius of gyration; MW, molecular weight; MM, molar mass; SEC-MALS, size exclusion chromatography−multi angle light scattering; MD, molecular dynamic; C.I., conservative index; rmsd, root mean standard deviation; IEF, isoelectric focusing; SDS−PAGE, sodium dodecyl sulfate−polyacrylamyde gel electrophoresis; FRET, Förster resonance energy transfer.

10.1021/bi8014967 CCC: $40.75

subunits (*13*). Each subunit of HSP16.5 and HSP16.9 comprises 1 ACD; instead, each of the 2 subunits of Tsp36 comprises 2 ACDs separated by a linker. Several other 3D structures have now been analyzed at lower resolution by cryoelectron microscopy (*14*−*18*). The α-crystallins, either native bovine (bαN) or recombinant hαA and hαB, were actively studied in solution (*18* and reviews in refs *19* and *20*). Moreover, a number of residues and peptides, specifically involved in subunit−subunit interactions and assembly, have been identified, thanks to the construction of a variety of mutants and the development of pin array analyses, coupled to the structural information available (*21*−*24*).

From a functional standpoint, it is generally accepted that the antistress function of the sHSPs relies on their chaperone-like activity, also associated with their dynamic quaternary structure and subunit exchange. These common structural and functional properties remain, however, compatible with tissue specific expression and specific target binding. Some of the sites involved in specific substrate associations of α-crystallins have been identified (*25*−*29*). Tertiary and quaternary structure appear, however, of utmost importance since, for instance, the 24-mer yeast HSP26 was observed to dissociate *in vitro* into dimers in heat shock conditions (*30*−*32*), whereas native α-crystallins (αN) required a doubling in size to associate the physiological substrates, β- and γ-crystallins, at the onset of their denaturation (*33*). We also demonstrated previously that, as far as the temperature induced structural transitions were concerned, αB alone did not behave as αN (*31*). Since, in addition, the R120G mutation is known for a long time to damage *in vitro* αB structure and chaperone-like activity (*34, 35*), and since a series of mutations at the R120 position had been observed recently to impair hαB behavior *in cellulo* (K, D, G, and C mutations) and hαB size *in vitro* (K, D, and G mutations since C was exclusively found in inclusion bodies) at ambient temperature (*36*), it was challenging to further investigate these R120 mutants. The present article started with the biophysical analysis of the temperature and pressure induced structural transitions of the three soluble hαB R120 mutants. Then, subunit exchange was analyzed using a new *in vitro* assay, in order to establish relationships between the quaternary structure or structural transitions and the αB dynamic properties. Finally, *in silico* models of the four R120 mutations were constructed in the dimeric substructures of the three available 3D structures (HSP16.5, HSP16.9, and Tsp36) in order to obtain clues on how these mutations may be responsible for structural destabilization and impaired function.

MATERIALS AND METHODS

Cloning, Mutagenesis, Expression, and Purification of hαB-WT and R120 mutants. The various steps from cloning to purification of all the hαB constructs have been recently described (*31, 33*−*36*). Briefly, sequences were cloned in pET24d (WT) or pET16b (R120 mutants) (Novagen) and transformed in *E.coli* BL21 strains. The expression was induced by the addition of 0.1 mM IPTG for 4 h at 37 °C. The purification protocol began with the cell wall disruption by the bug buster master kit (Novagen) supplemented with the protease inhibitor cocktail set VII (Calbiochem). The soluble protein fraction was obtained by centrifugation, then dialysed against 150 mM phosphate buffer at pH 6.8 (Buffer A = 22 mM Na_2HPO_4, 28 mM KH_2PO_4, 70 mM KCl, 1.3 mM EDTA, 3 mM NaN_3, and 3 mM DTT) with 0.6 mM PMSF (phenylmethylsulfonyl fluoride). In order to precipitate nucleic acids, 0.12% of PolyEthyleneImine (Qiagen) was added and then centrifuged. Finally, a single step of size exclusion chromatography on a Sephacryl S200 (GE Healthcare) was sufficient to obtain pure soluble proteins (as checked by SDS−PAGE and/or mass spectrometry). The purified proteins (always in buffer A, unless specified) were stored at 4° C. Concentrations were determined with a ND-1000 UV−visible spectrophotometer (NanoDrop Technologies), using an extinction coefficient ε (0.1%, 1 cm) of 0.69.

Dynamic Light Scattering (DLS). Hydrodynamic radii, (R_h), and percentages of polydispersity (% Pd) were measured by DLS using a DynaPro from Wyatt Technology Corporation (formerly Protein Solutions) using regularization methods (software Dynamics V6). The laser light wavelength was 830 nm, and the scattered light was collected at 90° by an optic fiber until it reached a detector. Temperature of the sample cell, from 4 °C up to 80 °C, was controlled with a Peltier element. As macromolecules are subjected to Brownian motions, their relative positions change as a function of time in a size-dependent manner. With solutions of identical particles, the calculation of the autocorrelation function of the measured scattered light as a function of time allows us to determine the diffusion coefficient of the species in solution, D_T. The hydrodynamic radius, R_h, is then calculated from the Stockes−Einstein equation according to the following:

$$R_h = K_B T / 6\pi D_T \eta \tag{1}$$

where K_B is the Boltzman constant, T the absolute temperature, and η the viscosity of the solvent (η is given by the program and is taken equal to 1.019 for the PSB buffer at 20 °C). With solutions of polydisperse yet monomodal particles, an average R_h is obtained in the same way, and the % Pd is calculated in addition. A monomodal DLS profile indicates the presence of a single population of structures in solution. This means that the size distribution can be ideally fitted by a Gaussian. When several species are present in solution, the number of species (≤ 3), together with the average R_h and polydispersity of each, can be determined, if the species present are sufficiently different (by regularization methods (*37*)). The technique was used to measure the hαB-WT and mutant size and polydispersity at ambient, 37, 48, 55, and 60 °C and to check the stability of these values as a function of time. All of the samples were filtered before experiments on Nanosep to eliminate large aggregates, dust particles, or bubbles. The protein concentration was measured and adjusted if necessary to be in the 0.1−1 mg/mL range (to get a sufficient signal-to-noise ratio and avoid the detector saturation), the sample volume 50 μL, the correlation time, τ, 0.5 μs, and the acquisition time for one measurement 10 s. Each experiment consisted of at least 20 up to 360 measurements. In some temperature experiments, the total scattered intensity, Is, was recorded. The following normalized scattered intensity, In, was used: $I\text{n} = (I\text{s at } T - \langle I\text{s at } T_0\rangle)/\langle I\text{s at } T_0\rangle$.

Small Angle X-ray Scattering (SAXS). Temperature and pressure induced oligomeric transitions were analyzed with

SAXS. Data collection was carried out at the ID2 beamline (*38*) at the European Radiation Synchrotron Facility (ESRF, Grenoble, France). The scattering intensity was measured with a 2D detector (fiber optically coupled FReLoN CCD based on Kodak image sensor) as a function of q, defined as $q = 2\pi s = (4\pi/\lambda)\sin\theta$, where s is the amplitude of the scattering vector, λ is the wavelength of the X-rays, and 2θ is the scattering angle. The sample to detector distance was set to 2 and 3 m.

The temperature experiments were performed at $\lambda = 0.0995$ nm (energy 12.4 keV), using a thermostatted ID2 flow-through cell (quartz capillary) filled and rinsed *in situ*, as previously described (*31*). Between two frames, fresh protein solution was pushed, using a remote controlled syringe coupled with the data acquisition program.

The pressure experiments were performed with the high-pressure cell and a biologically compatible sample holder as previously described (*31*). The spectra were recorded at higher energy (16.5 kev corresponding to $\lambda = 0.0751$ nm) in order to reduce the absorption coming from the diamond windows and the longer water path.

The protein concentrations varied from 3 to 8 mg/mL, to get a sufficient signal-to-noise ratio. The sample volume was 40−50 μL for the capillary experiments and 80−100 μL for the pressure one. The exposure time was chosen according to the protein concentration, the beam filling mode, and the experimental setup to obtain a sufficient signal-to-noise ratio and avoid the radiation damage from 0.1s to 3.0 s; 3 to 10 frames were recorded at each condition for the protein and 10 to 30 frames for the buffer. The 2D data reduction is described elsewhere (*39*).

The values of the intensity at the origin, $I(0)$, and of the radius of gyration, R_g, were derived from the scattering intensities, $I(q)$, using the Guinier approximation (*40*):

$$I(q) = I(0)\exp(-q^2R_g^2/3) \tag{2}$$

R_g and $I(0)$ were inferred, respectively, from the slope and the intercept of the linear fit of $\ln(I(q))$ versus q^2 at low q values ($qR_g < 1.0$). The particle molecular weight (MW in Da) or molar mass (MM in g/mol) and their changes occurring at the temperature or pressure induced transitions were followed from the variations of $I(0)$. An estimate of the particle size was obtained from R_g and its variations.

Size Exclusion Chromatography (SEC) and Multiangle Light Scattering (MALS). MM (or MW) determination was performed by SEC-MALS experiments immediately after sample preparation. Size exclusion chromatography was carried out on a silice KW 804 column (Shodex), connected to an AKTA Purifier chromatography system (GE Healthcare) with a three angle laser light scattering device and a refractive index detector (Treos Wyatt technology). Samples of 50 μL at around 1 mg/mL were used. All of the chromatography experiments were done at room temperature. In order to analyze temperature induced MW changes, the samples were preincubated for one hour at the desired temperature, cooled on ice for a few minutes (to block the subunit exchange process), and filtered at 4 °C for 10 min on Nanosep MF GFP 0.2 μm centrifugal devices (Pall life science) to eliminate dust particles, high MW aggregates, and bubbles prior to chromatography. Incubation temperatures were 4, 37, 48, 55, and 60 °C.

Anion Exchange Chromatography. Subunit exchange between hαB-WT or mutants and bαN (1:1 ratio) was further analyzed using 1 mL HiTrap ANX FF columns (GE Healthcare). The equilibration buffer was 20 mM Tris at pH 6.8, and the elution buffer was the same including 1 M NaCl. These buffers were chosen to be able to separate the hαB-WT (pI = 6.8, not retained on the column) from the bαN (pI = 5.6, eluting around 29.5% NaCl) and possibly exchanged intermediate species. The elution was done at ambient temperature, the elution rate was 1 mL/min, the injected volume was 100 μL, and the gradient was fixed at 1.5% per mL. The protein concentration range was from 1 to 2 mg/mL. After mixing at 4 °C where exchange does not take place, the samples were directly injected (0 h) or preincubated at 37 °C for different times, typically 1, 3, 5, 16, and 24 h, before loading on the anion exchange column.

Multiple Sequence Alignment. The multiple sequence alignment of the N-terminal domain N-ter), α-crystallin domain (ACD), and C-terminal extension (C-ter) of 6 sHSPs was achieved: *Methanococcus jannaschii* HSP16.5 (pdb code: 1SHS; Swiss-Prot accession number: Q57733), *Triticum aestivum* HSP16.9 (1GME; Q41560), *Taenia saginata* Tsp36 (2BOL; Q7YZT0), and *Homo sapiens* HSP27 (P04792), HSP22 (Q9UJY1), αA (P02489), and αB (P02511). Tsp36 comprises one N-ter domain, two ACDs separated by a linker (41 amino acids), followed by one C-ter extension. The sequences of the N-ter and C-ter regions were manually aligned. The multiple alignment of the ACD sequences was achieved by MUSCLE ((*41*); http://www.drive5.com/muscle); the available 3D structural data were also taken into account in order to align the sequences of the L57 loop (between the B5 and B7 β-strands).

In Silico Site-Directed Mutagenesis. Dimer mutants were generated by amino acid replacement (with K, D, C, or G) in each 3D coordinate file (1SHS, 1GME, and 2BOL) at the R position of the A chain equivalent to the αB-crystallin R120 position (107 in 1SHS, 108 in 1GME, 158 in 2BOL), as follows; note that the second ACD in the Tsp36 sequence shares a lysine at this homologous site and is therefore not concerned by this amino acid replacement. For each protein, the PHYRE threading program was used first ((*42*); http://www.sbg.bio.ic.ac.uk/phyre); PHYRE uses a rotamer library to attach the amino acid side chain along the backbone to avoid clashes and simultaneously attain an energetically favorable and compact arrangement. The second step consisted in the fit of the monomer (mutant model or wild-type chain A) on the 3D coordinates of the second monomer involved in the dimer (1SHS C chain, 1GME and 2BOL B chain). We thus obtained a dimeric substructure composed of two identical monomers, composed of 1 ACD surrounded by a N-ter domain and a C-ter extension for 1SHS and 1GME, or of 2 ACDs separated by a linker and surrounded by a N-ter domain and a C-ter extension for 2BOL (indeed, part of the N-ter region was not visible in the 1GME B chain, and the L57 loop was not visible either in the first ACD of the 2BOL B chain). Fitting was performed using the McLachlan algorithm (*43*), as implemented in the program ProFit (Martin ACR and Porter C.T.; http://www.bioinf.org.uk/software/profit).

The GROMACS package ((*44*); http://www.gromacs.fr) was then used to center and solvate each dimer (wild-type or mutant, partial or complete) in a cubic box with explicit solvent (water). Energy minimization by the steepest descent method, followed by the conjugate gradient method was used to remove bad contacts and reduce the potential energy of each system. The dimers and their mutants were negatively charged; each system was neutralized by the replacement of *n* water molecules by *n* sodium counterions (1SHS, $n_{WT/K} = 8$, $n_D = 12$, $n_{G/C} = 10$; 1GME, $n_{WT/K} = 2$, $n_D = 6$, $n_{G/C} = 4$; 2BOL: $n_{WT/K} = 14$, $n_D = 18$, $n_{G/C} = 16$).

Simulated Annealing. Molecular dynamic (MD) simulations on the dimeric substructures were carried out using the GROMOS energy function (GROMOS96 43a1 force field). Solvent equilibration was first achieved by a 20 ps MD simulation at 300 K: the solvent was relaxed, while the dimer was kept frozen, using 2 fs time steps; in subsequent MD simulations, each system was heated from 300 to 600 K in 1 ps, equilibrated for 1 ps and then cooled in 4 ps from 600 to 300 K (with 1 fs time steps); this 6-ps simulated annealing process was repeated 100 times. Snapshots and averaged atomic coordinates were taken every 0.5 ps; the collected data were used for the analysis of both contact sites and structural fluctuations.

Contact Analysis. The intra and intermolecular hydrogen-bonds (atomic distance <3.6 Å) involving atoms of the residue 120 were computed by the program Contact implemented in the CCP4 package ((*45*); http://www.ccp4.ac.uk).

Analysis of the Structural Fluctuations. For each system, rmsd values (root-mean-square deviation, which is the average distance between atoms of superimposed structures) were computed between each time-specific structure (or substructure) and the initial one after minimization (0 ps of the MD simulation; *g_rms*, GROMACS package). We have also computed the mean and the standard deviation of the rmsd values, among the 100 time-specific structures with the lowest potential energy (i.e., the 100 cooled structures collected at 6*n* ps of the MD simulation). Indeed, the rmsd values were computed between the given time-specific structure and the corresponding one after the first minimization (0 ps of the MD simulation), for both backbone and side chain atoms: 6 Å (WT), 6.4 Å (K), 6 Å (D), 8.2 Å (G), and 8 Å (C); these values are characteristic of each system during the MD simulations. The structures that have their rmsd as close as possible to the average rmsd may not correspond to the same number of cycles. Indeed, for the WT it was obtained after 28 cycles (168 ps) of simulated annealing, and the following values were obtained for the mutants: K (39 cycles, 234 ps), D (70 cycles, 420 ps), G (81 cycles, 486 ps), and C (66 cycles, 396 ps). For each, statistical analysis of variance values were achieved (Anova in the R package; http://www.r-project.org/) in order to test whether the mean of the rmsd values of WT and mutants do significantly differ.

RESULTS

Assembly State and Polydispersity Analysis As a Function of Temperature by DLS. The hαB-WT and R120 mutants (the soluble ones: R120K, R120D, and R120G) were investigated with DLS as a function of temperature to determine the hydrodynamic radii (R_h) and the percentages of polydispersity (% Pd). The stability of the different proteins was also followed as a function of time. To analyze the temperature induced structural modifications, the R_h and the % Pd were measured at each temperature of interest.

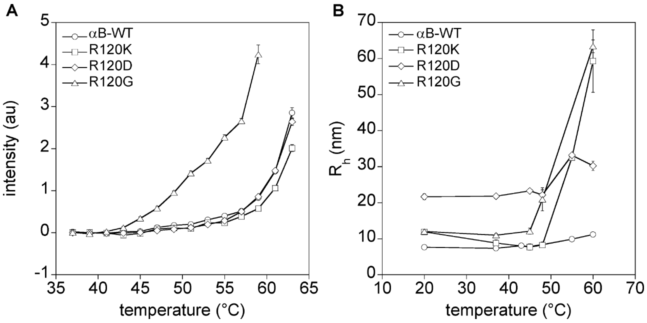

FIGURE 1: DLS analysis of (○) hαB-WT, (□) R120K, (◇) R120D, and (Δ) R120G mutants as a function of temperature. (A) Kinetic experiments: the total scattered intensity was measured every 2 °C from 37 to 63 °C, for 200 s (20 points at 10 s each). (B) Static experiments: the R_h values were calculated after equilibration of each sample for 1010 s at the chosen temperature and averaged over the different preparations.

DLS is a versatile approach that can be used in different ways. A rapid exploration of the system was done in the following way: after equilibration of the sample at physiological temperature for 15 min, the total scattered intensity was measured every 2 °C from 37 to 63 °C, for 200 s (20 points at 10s each, Figure 1A). This total scattered intensity originates from the scattering of the particles of interest and from their associations. In the following, we distinguish the changes in size or number of subunit reproducibility induced by increasing the temperature (called the temperature induced transitions), from the uncontrolled formation of high MW aggregates of denaturated materials. In particular, the DSL intensity is sensitive to the formation of high MW, yet soluble, species or aggregates, and increases rapidly as soon as such aggregates are formed. As already described (*36*), the size distribution profiles at ambient temperature (not shown) were rather different for hαB-WT and for the mutants. The mutant size distribution profiles were much more asymmetrical, indicating the presence of a significant fraction of particles with large sizes and MW. The presence of aggregates ($R_h \geq$ 100nm, not shown) may be detected as early as 43 °C with the R120G mutant, at 59 °C for the hαB-WT and the R120D mutants and around 61 °C for the R120K mutant.

In another series of experiments, the sample holder was first equilibrated at the desired temperature: ambient, 37, 45, 48, 55, or 60 °C. Then the sample was placed in the sample holder, and the autocorrelation function was recorded continuously as a function of time over a 1 h period (360 points, 10 s each) or until the detector saturation for the highest temperatures, allowing us to calculate R_h and % Pd afterward at any time. Fresh samples were used at each temperature. Until 50 °C, the equilibration occurred in about 10 min, and then the system remained stable for at least 1 h. The R_h and % Pd values were finally compared, after 1010 s. The values observed at different temperatures for the different hαB and averaged over the different preparations, are given in Table 1. The R_h are plotted in Figure 1B. The preparations that gave unexpectedly large R_h values (1 out of 12 for the hαB-WT and up to 5 out 12 for R120G) were not taken into account.

Between ambient temperature and about 45 °C, the R_h values at the maximum of the distribution were found to increase in the following order: hαB-WT < R120K <

Table 1: DLS Data[a]

temperature		ambient	37 °C	45 °C	48 °C	55 °C	60 °C
hαB-WT	R_h (nm)	7.6 (0.1)	7.3 (0.1)	7.8 (0.1)	8.3 (0.2)	9.8 (0.2)	11.2 (0.3)
	% Pd	29.7 (2.8)	21.5 (1.4)	21.3 (1.8)	21.6 (6.8)	36.8 (4.2)	23.0 (2.0)
R120K	R_h (nm)	11.9 (0.6)	8.7 (0.9)	7.6 (0.8)	8.2 (0.6)	32.5 (0.1)	59.3 (8.6)
	% Pd	35.7 (3.0)	21.4 (3.8)	17.6 (2.5)	17.7 (4.9)	39.9 (1.1)	24.3 (3.7)
R120D	R_h (nm)	21.6 (0.8)	21.8 (0.5)	23.3 (0.3)	22.1 (1.4)	33.2 (0.5)	30.2 (1.3)
	% Pd	39.0 (3.6)	46.5 (5.1)	47.7 (4.4)	43.6 (1.5)	43.3 (2.6)	27.1 (4.7)
R120G	R_h (nm)	12.0 (0.4)	10.9 (0.5)	12.1 (0.8)	20.9 (3.2)	N.D.	63.4 (1.8)
	% Pd	34.7 (4.7)	37.4 (5.4)	51.6 (3.5)	53.5 (2.8)	N.D.	29.7 (2.4)

[a] Average R_h values and % of Pd after an equilibration time of 1010 s at the chosen temperature. The standard errors are given in parentheses. N.D.: not determined.

R120G < R120D. The % Pd was increasing in the same order. The hαB-WT, the R120K, and R120D mutants were found to remain stable at 4 °C for several days. On the contrary, the R120G mutant was forming whitish precipitates sedimenting at the bottom of the tube in a few days.

As can be seen in Figure 1B and Table 1, the size and polydispersity of the hαB-WT was minimum at 37 °C (the total scattered intensity was also minimum at 37 °C). The R_h of the hαB-WT, 7.3 nm at 37 °C, started to slowly increase after 40 °C, to reach 11.2 nm at 60 °C. The polydispersity increased at the same time. The irreversible formation of large aggregates (>50nm) was observed after 60 °C. Each mutant behaved in its own and different way. The R_h of the R120K mutant first decreased until about 45 °C from 11.9 to 7.6 nm, possibly owing in part to the decrease in polydispersity, and then increased rapidly up to 32.5 nm at 55 °C indicating a rapid transformation of the initial particle population into much larger species. After 48 °C, the system was unable to differentiate the particles and the growing aggregates, and the measured R_h was an average taken over a wide range of species of different sizes. The R_h of the R120D mutant remained stable around 22 nm up to 48 °C, then increased until 33.2 nm at 55 °C, indicating the growth of larger species. The R_h then decreased again, probably owing to the sedimentation of these larger species outside the laser beam. All of the changes observed were found irreversible. The R120G mutant behaved differently. The mutant R_h decreased from 12.0 nm at ambient temperature to 10.9 at 37 °C and remained stable until 45 °C. The R_h then increased because of the formation of high MW aggregates, increasing as a function of time.

Temperature Induced Transitions as Observed by SAXS. The SAXS intensity curves of the hαB-WT and the 3 mutants were recorded as a function of temperature from ambient to 60 °C. The evolution of the scattering curves as a function of temperature are shown in Figure 2A−D, and the scattering curves of the hαB-WT and the 3 mutants at ambient temperature are compared in Figure 2E. The evolution of the corresponding radius of gyration (R_g), as a function of temperature, is plotted in Figure 2F.

In this series of curves, the protein concentrations were in between 3−8 mg/mL to obtain a sufficient signal-to-noise ratio. The curves can be considered to be close to the form factor, as shown at ambient conditions in Figure 2E: the shapes of the scattering curves were typical of globular particles, with size and polydispersity increasing in the order hαB-WT < R120K < R120D ∼ R120G. Indeed, the width of the central maximum was found to decrease and R_g to increase according to this order (the R_g values were found to be, respectively, 6.1 nm, 7.5 nm, 9.2 nm, and 9.5 nm).

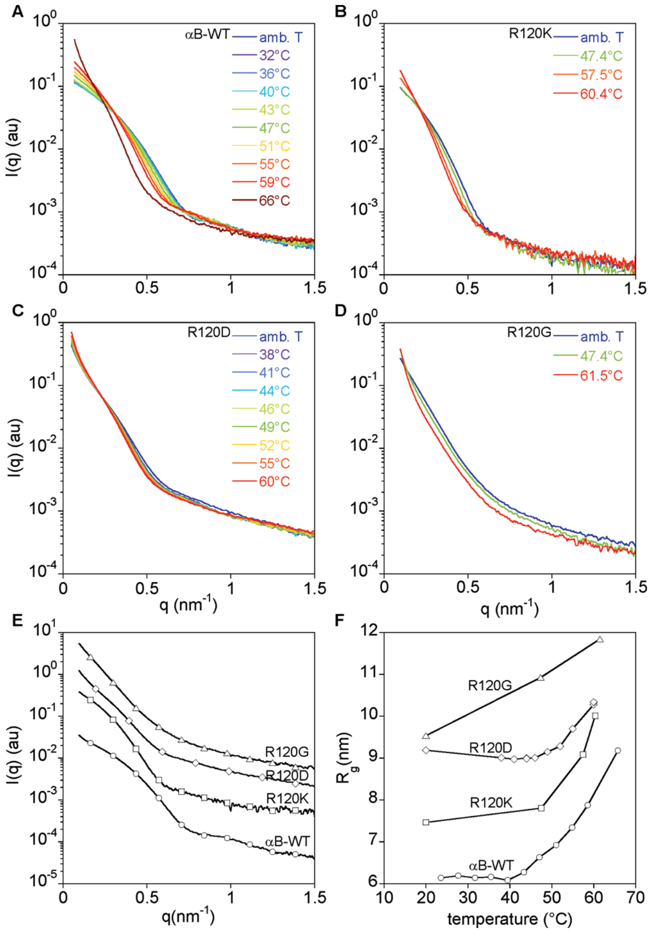

FIGURE 2: Temperature induced structural transitions as observed by SAXS. Temperature scans at ambient pressure of (A) hαB-WT, (B) R120K, (C) R120D, and (D) R120G mutants. The normalized X-ray scattering intensities were recorded as a function of the scattering vector q between ambient temperature and 66 °C at P = 0.1 MPa (1 atm). (E) Normalized X-ray scattering intensity curves of (○) hαB-WT, (□) R120K, (◊) R120D, and (Δ) R120G mutants at ambient temperature and pressure. For the sake of clarity, the curves were vertically shifted. (F) Corresponding R_g values as a function of temperature.

Also, after the central maximum, the hαB-WT exhibited a shoulder around $q = 1$ nm^{-1}. The shoulder is a rough indication of polydispersity since it becomes more pronounced when polydispersity decreases. It was barely visible with the R120K mutant and had disappeared with R120D and R120G, as expected with an increasing polydispersity. The presence of a few percent of large particles in the R120D and R120G samples can also be guessed from the increase of the scattering curves near the origin.

Size and MW of the hαB-WT were stable until 40 °C and then were seen to increase with temperature (Figure 2A). The increase was continuous until 59 °C (*31*). At 59 °C, MW, as estimated from the $I(0)$ value (not shown), was about twice the initial MW, and R_g was 7.9 nm as compared to 6.1 nm at 20 °C. The transition was irreversible. Above 60 °C, the formation of large aggregates (sedimenting at the bottom of the tube) was observed. A minimum of polydispersity, estimated from the shape of the shoulder around $q = 1$ nm^{-1}, could be observed around 37 °C. As seen from Figure 2B, the R120K mutant behaved in a similar way, with a R_g value rather stable until 48 °C, but starting from a higher R_g (7.5 nm at 20 °C and 7.8 nm at 48 °C) and increasing afterward, up to 9.1 at 58 °C. Yet the change in size was less important than that for hαB-WT since R_g increased about 17% between 48 and 58 °C instead of 30% for the hαB-WT between 40 and 59 °C. The temperature induced transition of the R120D mutant (Figure 2C) was even more restricted, with R_g increasing from 9.1 nm up to 10.2 nm between 48 and 60 °C (12%). All of these data were in agreement with the DLS results and complemented them. The R120G mutant (Figure 2D) was visibly contaminated with aggregates even at ambient temperature, probably because protein purification had to be prepared a few days before the X-ray experiments. The corresponding R_g, equal to 9.5 nm at 20 °C increased up to 11.8 at 61 °C. In this case, it remained unclear whether a temperature induced transition, i.e., a temperature controlled size increase, was present, or the changes observed near the origin of the scattering curves from ambient temperature were already due to the formation of large aggregates (corresponding to the first step toward uncontrolled precipitation of denatured material).

Pressure Induced Modifications as Observed by SAXS at Ambient Temperature. The pressure scans for hαB-WT, R120K, and R120G are shown in Figure 3A, B, and C and the corresponding R_g in Figure 3D from ambient pressure to 300 MPa. R120D was precipitated and could not be studied during the experiment at the synchrotron. In all three cases, two effects are superimposed: (i) the overall scattering intensity decreases as the pressure increases, reflecting the decrease of the contrast between protein and solvent; (ii) the pressure induced structural modifications observed between ambient pressure and 300 MPa mimic the temperature induced modifications observed between room temperature and 60 °C. For hαB-WT, the transition roughly corresponded to a doubling in size. The transition was, however, fully reversible with some hysteresis as can be seen on Figure 3D. The size of the R120K mutant also increased with pressure yet was relatively less (Figure 3B and D). As with temperature, the maximum R_g increase was about 20%, although the transition was essentially reversible. Finally, the changes observed for the R120G scattering curves were the most difficult to interpret since they were consistent with a simultaneous increase in size and in polydispersity or, in other words, with the formation of larger aggregates. The changes, at the limit between transition and precipitation, were only partially reversible. In all cases, the high pressure state was similar to the high temperature state, in agreement with what is expected for equilibrium states.

Some pressure experiments were also performed at other temperatures, 37 and 48 °C (not shown). Essentially, the pressure induced contrast variation between protein and solvent was reduced at higher temperatures. The pressure effect then was enhanced at higher temperatures yet, with the mutants, the higher temperature seemed to favor the irreversible formation of a variable percentage of high MW aggregates, competing with the reversible high MW assemblies corresponding to a reversible structural transition. In the case of hαB-WT, the combination of high temperature (43.5 °C) with pressure, favored the reversible structural transition (*31*).

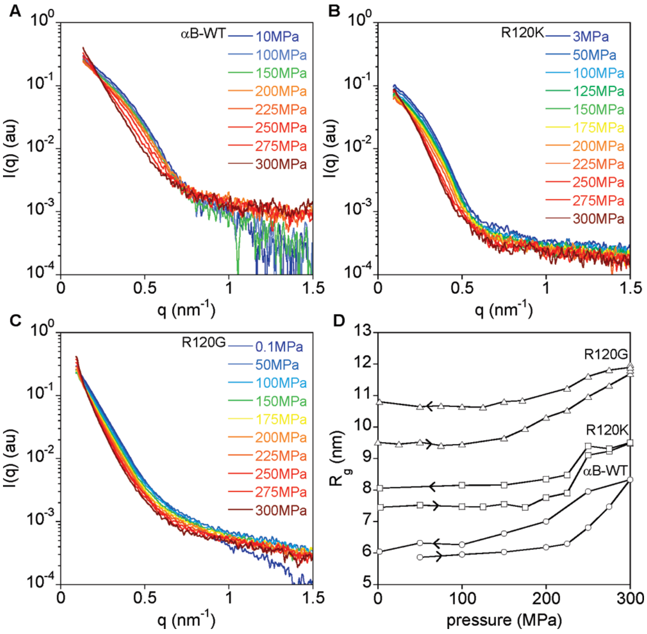

FIGURE 3: Pressure induced structural transitions as observed by SAXS. Pressure scans at ambient temperature of (A) hαB-WT, (B) R120K, and (C) R120G mutants. The normalized X-ray scattering intensities were recorded between 0.1 and 300 MPa (1 and 3000 atm). (D) Corresponding R_g values as a function of pressure. A complete hysteresis cycle is shown. The lower points were recorded during the pressure increase; the upper points correspond to the return to ambient pressure, as indicated with the arrows.

Molecular Weight Determination as a Function of Temperature by SEC-MALS. Differential refractive index profiles of purified hαB were measured by SEC-MALS as a function of incubation temperature in order to determine the corresponding MM (or MW). The results are given in Figure 4A for the hαB-WT and Figure 4B for the R120K from ambient to 55 °C. After 1 h at 60 °C, a significant part of the protein formed high MW aggregates, which were eliminated in part by the filtration step. The remaining soluble part eluted at around 2400 kDa, close to the void volume (not shown). The averaged value of the MW and the estimated averaged number of subunits are reported in the Table 2. In the case of the R120D and the R120G mutants, the profiles obtained at ambient temperature already indicated very large MW and polydispersities, with a significant part of the sample eluting in the void volume (not shown). These parameters were no more pertinent, and the temperature evolution was not pursued.

For hαB-WT and for R120K, as can be seen on the Figure 4A and B and Table 2, no significant evolution of the samples occurred between 4 °C, the storage temperature, and 20 °C, the temperature of the chromatography experiment, and the variation of the MW with temperature confirmed that the

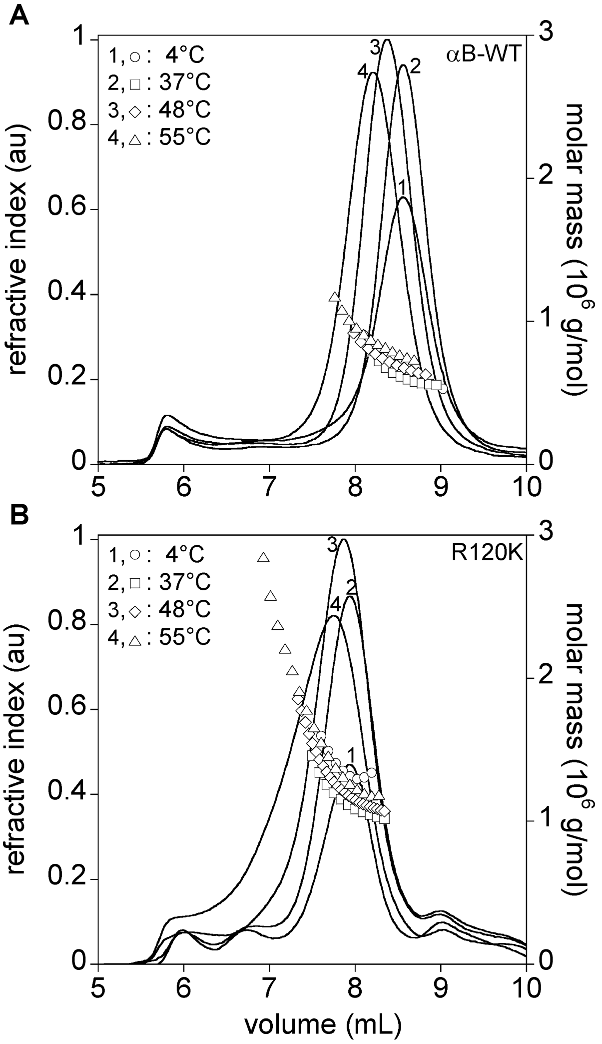

FIGURE 4: SEC-MALS experiments. Differential refractive index elution profiles (continuous lines) of (A) hαB-WT and (B) R120K mutant, and corresponding molar masses (symbols). Each sample was incubated for 1 h at the chosen temperature (1, 4 °C; 2, 37 °C; 3, 48 °C; 4, 55 °C) before injection on the column.

Table 2: Summary of SEC-MALS Data[a]

temperature		4 °C	37 °C	48 °C	55 °C
hαB-WT	MM (10^3 g/mol)	646	623	734	886
	SU nb	32 [26−46]	31[27−41]	36 [31−47]	44 [35−60]
R120K	MM (10^3 g/mol)	1307	1151	1275	1694
	SU nb	65 [63−82]	57 [50−75]	63 [52−93]	84 [58−161]

[a] Weighted average molar mass (MM) values of hαB-WT and R120K mutant, and the number of subunits calculated with subunit MM, respectively, of 20.1589 and 20.1309 10^3 g/mol (kDa). Limits are given in parentheses. Each sample was incubated for 1 h at the chosen temperature before injection.

temperature induced changes were not reversible. The MW of hαB-WT were found to be similar at 4 and 37 °C and equal, respectively, to 646 kDa and 623 kDa, corresponding to 32 and 31 subunits in average. The MW then regularly increased as a function of temperature, to reach 734 kDa at 48 °C and 886 kDa at 55 °C (44 subunits in average). The same experiments, performed with the R120K mutant (Figure 4B), showed that the R120K assembly exhibited a higher MW compared to that of the wild type, as previously shown by DLS and SAXS. The estimated MW corresponded to 1307 kDa at 4 °C, 1151 at 37 °C, 1275 at 48 °C, and 1694 at 55 °C (up to 84 subunits). The overall evolution of this mutant appeared similar to hαB-WT, yet the formation of aggregates started earlier, around 55 °C, and was overwhelming at 60 °C. The lower MW observed at 37 °C, as compared with 4 °C, corresponded to a smaller polydispersity of the samples at physiological temperatures, as already observed by DLS and SAXS.

*Subunit Exchange of h*αB*-WT and Mutants Investigated by Anion Exchange Chromatography.* To identify subunit exchange, in concentration conditions similar to those used for DLS and SAXS, conditions leading to new particles with different sizes or charges were looked for. We choose to use bαN as the exchanger, for its high stability and charge difference with hαB. Two different approaches, sensitive to changes in charge, were tested. The first one was direct visualization of the new particles formed with IEF gels. Although the technique was successfully used to follow the exchange between hαB-WT and bαN (not shown), the mutant sizes were found too large to reproducibly migrate in the IEF gels and the experiments were not pursued. The second method, the anion exchange chromatography with Hi-Trap ANX 1 mL columns, was preferred to measure the subunit exchange of hαB-WT and R120 mutants with bαN. A 1:1 ratio was chosen for all experiments.

In a pH 6.8 buffer, hαB-WT, that has an isoelectric point (pI) close to the buffer pH, is not expected to be retained on the column. However, bαN, which has a pI around 5.2, is eluted only by the addition of salt. Indeed, in the gradient conditions used, hαB-WT eluted in the void volume, whereas bαN eluted at the end (29.3−29.6%) of the NaCl gradient. It was first checked that the elution profiles for bαN alone and for each (WT and mutants) of the hαB samples were the same when the injection was done with samples kept at 4 °C and with samples incubated alone at 37 °C for 24 h. It was also checked that exchange within the mixtures of bαN and hαB did not occur at 4 °C and remained marginal at ambient temperature after 24 h of incubation. These necessary controls allowed us to perform the chromatography experiments (that last for about 50 min) at ambient temperature. The hαB and bαN mixtures were then incubated at 37 °C, and the reactions were stopped at will by putting the samples on ice for a few minutes, after incubation times from 1 h up to 24 h. Figure 5A shows the exchange experiment as a function of incubation time for an hαB/bαN mixture. A 1:1 ratio was chosen for all experiments. As can be seen in the figure, a new peak eluted before the bαN peak, indicating that exchange was taking place and that a new mixed population was formed and was measurable by this technique. Subunit exchange was found already significant after 1 h of incubation time, and only one type of particles was visible after 5 h. It was verified by SDS−PAGE (not shown) that the new particles indeed contained both hαB-WT and bαN: αA and αB give two distinct bands, whose intensities can be directly correlated to the protein ratio. A few experiments were performed with incubations at 40 °C (not shown). As expected, for identical incubation times the exchange was found to occur faster.

Subunit exchange between bαN and the R120 mutants were measured in the same way and the results shown in Figure 5B, C, and D. Subunit exchange was found to occur faster between bαN and the mutants than versus hαB-WT.

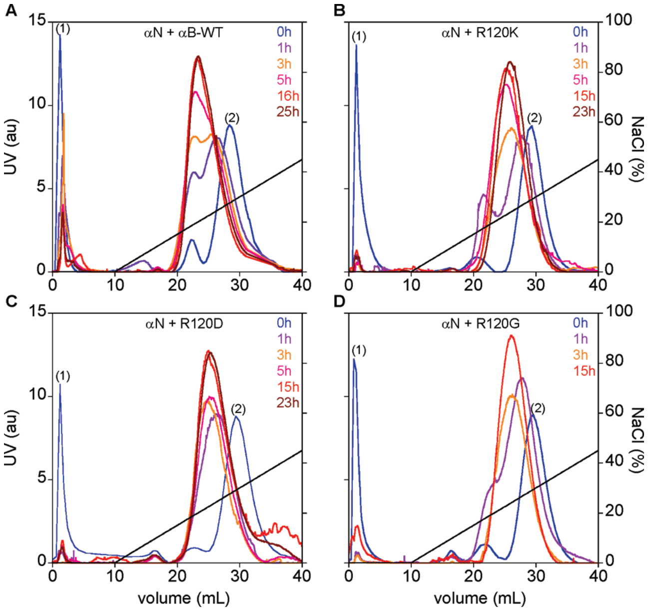

FIGURE 5: Subunit exchange capacity of hαB-WT and R120 mutants using anion exchange chromatography. Elution profiles (UV 280 nm) with NaCl gradient of mixtures of bαN and (A) hαB-WT or (B) R120K, (C) R120D, and (D) R120G mutants incubated at 37 °C for different times as indicated. The protein ratio was 1:1. In the absence of incubation at 37 °C (0 h), hαB-WT (1) or R120 mutants were not retained on the column, whereas bαN (2) eluted around 29 mL (29.5% NaCl).

With R120K and R120G, only one peak was visible after 3 h of incubation at 37 °C, and 1 h was sufficient for R120D.

In Silico Analysis. Direct visualization of the three known 3D structures indicated that the R residue equivalent to the αB-WT R120 and its local environment were equivalent (similar intramolecular contacts) and correctly superimposed at the monomer level. In the dimeric substructures of HSP16.5 and HSP16.9, this residue is also involved in ACD/ACD intermolecular interactions. This interface (that one may assume to be characteristic of the α-crystallin superfamily) is not observed in Tsp36, neither between its 2 subunits nor between the 2 ACDs of a given subunit. The multiple sequence alignment of HSP16.5, HSP16.9, Tsp36, HSP27, HSP22, hαA, and hαB was then performed on the total sequences in order to locate the residues involved in the equivalent R120 environment. The hαA, HSP22, and HSP27 sequences, where mutations responsible for inherited human pathologies were known, were included in the alignment. The multiple alignment of the ACD is fully coherent with the already published ones (*12, 13*). Because of the low sequence identity in the N-ter domain, the alignment in this part was only tentative but not critical for the R120 environment. The result is shown in Figure 6A.

To further analyze the possible impact of R120 mutations on structural integrity and assembly, mutants of the dimer substructure were generated *in silico* by amino acid replacement (with K, D, C, or G, C was also included in the series) in each 3D coordinate file (1SHS, 1GME, and 2BOL) at the critical R position, as indicated in Materials and Methods. For each system, 6 ps MD simulations were carried out in order to explore the energetical landscape (and assume, for HSP16.5 and HSP16.9, which regions of the conformation space may be explored by a given dimer during the assembly) and the simulated annealing process repeated 100 times. Then, the 20 structures with the lowest potential energy were retained from the 100 cooled structures, and the contact sites involving the residue at the equivalent 120 position were defined as those where H-bonds were detected according to atomic distances. We have defined and computed a conservative index (C.I.) for each contact site, as the number of structures (among the 20) where the given H-bond was observed. The list of contacts observed, and the corresponding conservative index, for the 20 structures of HSP16.9, HSP16.5, and Tsp36, and, in each case, for the WT and the K, D, G, and C mutants, are given in Table 3.

Examples of the dimeric substructures observed for HSP16.5 WT (as in the pdb file) and the WT and mutants during the simulated annealing process are shown in Figure 6B. HSP16.5 was chosen as an example since its sequence in the equivalent R120 environment was the most similar to that of hαB. The first structure displayed corresponds to the dimer from 1SHS. Then, each substructure displayed corresponds to the structure (among the 100 structures with the lowest potential energy) having the average root-mean-square deviation, rmsd (i.e., mean value or within the standard deviation).

The contacts observed in the 1SHS pdb structure were the following: I37, S38, G39, K40, G41, F42, M43, L77, I79, and E98 (the only intermolecular contact site). These contacts were essentially conserved during the annealing process in the WT (R in Figure 6B) substructure. Instead, as can be seen in the table for the four mutant substructures considered, large contact perturbations were observed. Yet, the R and the K substructures preserved similar contact regions, with intrasubunit contacts in the B1, L12 (or equivalent), and B5 regions, and intersubunit contacts in L57, whereas the intersubunit contact was lost with the D, G, and C mutations. Contacts in the L12 loop disappeared with mutations G and C, and finally the G mutant lost the B1 contacts. The 1GME case behaved in a similar way, i.e., only the K mutation conserved the intersubunit contact, which was lost for all mutations with 2BOL.

DISCUSSION

The Arg residue at position 120 is known to play a crucial role in the quaternary structure control and functional integrity of hαB-WT (*34, 36, 46−48*). In the present study, complementary techniques, DLS, SAXS, SEC-MALS, and subunit exchange assays were combined to investigate and compare, as a function of the environment and in stress conditions, the assembly state, the conformational transitions, and the subunit exchange capacity of hαB-WT and of different R120 mutants: the pathological R120G and the constructed R120K and R120D mutations. Additional information was obtained on mutant stabilities and their propensities to form high MW aggregates or insoluble precipitates. Finally, MD simulations of the mutants of the three known 3D structures (site-directed mutagenesis at the R120 equivalent position) suggested that the observed behavioral modifications could result from a mutation induced destabilization of the local environment; in the HSP16.5 and HSP16.9 structures, this destabilization could lead to the perturbation of the ACD/ACD interface of the dimeric substructure.

Special attention was paid in this study to optimize the available tools. DLS and SAXS were extensively combined

A

```
N-ter
HSP16.5_METJA    1 ------------MFGR-------DPFDS--LFERMFKEFFATPMTGTTMIQ----------------------------------------SSTGIQISGKGFMP-----  44
HSP16.9_TRIAE    1 MSI-----------VRR---------------TNVFD-PFADLWADPFDTFRSIV------------------------------PAISGGGSETAAFAN-AR-------  45
Tsp36_TAESA      1 MSIFPTRDSRDLSSRRRSLIDWEFPQMALVPLDQVFD--WAERSRQSLHDDIVNM-----HRNLFSLEPFTAMDNAFESVMKEMSAIQPREFHPELEYTQPGELDFLKDA 103
HSP27_HUMAN      1 ----MTERRVPFSLLRGPSW---DPFRDWYPHSRLFDQAFGLP---RLPEE----WSQW----LGGSSWPGYVRPLPPAAIESPAVAAPAYSRALSRQLSSGV-------  85
HSP22_HUMAN      1 ----MADGQMPFSCHY-PSRLRRDPFRDSPLSSRLLDDGFGMD---PFPDDLTASWPDWALPRLSS-AWPGTLRSGMVPRG------PTATARF-GVPAE-GR-------  86
Cryst-A_HUMAN    1 ---MDVTIQHPW--FKRTLG----PFY----PSRLFDQFFGEG---LFEYDLLPF--------LSSTISPYY-R--------------QSLFR--T-VLDSGI-------  61
Cryst-B_HUMAN    1 ---MDIAIHHPW--IRRPFF----PFHS---PSRLFDQFFGEH---LLESDLFP---------TSTSLSPFYLR-------------PPSFLRAPS-WFDTGL-------  65

ACD                B2     L23     B3      L34         B4     L45 B5      L57                   B7      L78        B8    L89 B9
HSP16.5_METJA   45 ISIIEG D-----Q HIKVIAW LP---GVNKED IILNAV G-D TLEIRAK RSPLMITESERIIYSEIPEEE EIYRTIK LPATVKEENA SAKFE N-G VLSVILP 134
HSP16.9_TRIAE   46 MDWKET P-----E AHVFKAD LP---GVKKEE VKVEVE DGN VLVVSGE RTKEKEDKNDKWHRVERSSG- KFVRRFR LLEDAKVEEV KAGLE N-G VLTVTVP 135
Tsp36-1_TAESA  104 ----YE VGKDGRL HFKVYFN VK---NFKAEE ITIKAD K-N KLVVRAQ KSVACGDAAM---------SE SVGRSIP LPPSVDRNHI QATIT TDD VLVIEAP 186
Tsp36-2_TAESA  228 ----AE D-----G SKKIHLE LKVDPHFAPKD VKVWAK G-N KVYVHGV TGKEEKTENA-----SHSEHR EFYKAFV TPEVVDASKT QAEIV D-G LMVVEAP 311
HSP27_HUMAN     86 SEIRHT A-----D RWRVSLD VN---HFAPDE LTVKTK D-G VVEITGK HEERQDEHGY--------ISR CFTRKYT LPPGVDPTQV SSSLS PEG TLTVEAP 168
HSP22_HUMAN     87 TPPPFP G-----E PWKVCVN VH---SFKPEE LMVKTK D-G YVEVSGK HEEKQQEGGI--------VSK NFTKKIQ LPAEVDPVTV FASLS PEG LLIIEAP 169
Cryst-A_HUMAN   62 SEVRSD R-----D KFVIFLD VK---HFSPED LTVKVQ D-D FVEIHGK HNERQDDHGY--------ISR EFHRRYR LPSNVDQSAL SCSLS ADG MLTFCGP 144
Cryst-B_HUMAN   66 SEMRLE K-----D RFSVNLD VK---HFSPEE LKVKVL G-D VIEVHGK HEERQDEHGF--------ISR EFHRKYR IPADVDPLTI TSSLS SDG VLTVNGP 148

C-ter
HSP16.5_METJA  135 -------KAESSIKKGINIE--------------------- 147
HSP16.9_TRIAE  136 -----KAEVKKPEVKAIQISG-------------------- 151
Tsp36_TAESA    312 LFK-------------------------------------- 314
HSP27_HUMAN    169 ----MPKLATQSNEITIPVTFESRAQLGGPEAAKSDETAAK 205
HSP22_HUMAN    170 QVPPYSTFGESSFNNELPQDSQEVTCT-------------- 196
Cryst-A_HUMAN  145 --KIQTGLDATHAERAIPVSREEKP--TSAPSS-------- 173
Cryst-B_HUMAN  149 ------RKQVSGPERTIPITREEKPAVTAAPKK-------- 175
```

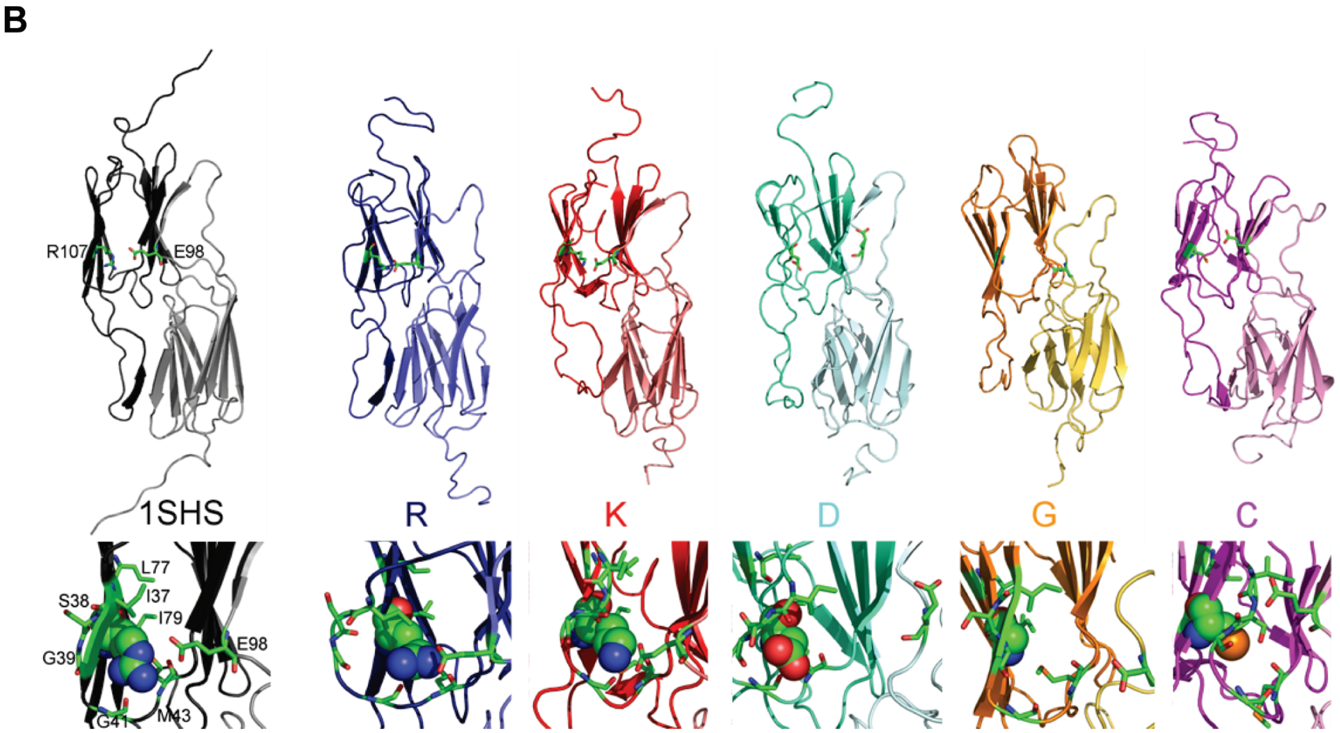

FIGURE 6: Structural consequences induced by the R120 mutations: *in silico* analysis. (A) Multiple sequence alignment of the N-terminal region (N-ter), α-crystallin domain (ACD), and C-terminal region (C-ter) of 6 sHSPs: *Methanococcus jannaschii* HSP16.5 (PDB code, 1SHS; Swiss-Prot accession number: Q57733), *Triticum aestivum* HSP16.9 (1GME; Q41560), *Taenia saginata* Tsp36 (2BOL; Q7YZT0), and *Homo sapiens* HSP27 (P04792), HSP22 (Q9UJY1), αA-crystallin (P02489), αB-crystallin (P02511) (see Material and Methods for details). Tsp36 comprises one N-ter domain, two ACDs separated by a linker (sequence not shown), followed by one C-ter extension; Tsp36−1 and Tsp36−2 refer to the first and second ACD sequences, respectively. In italic are the amino acids absent from the 3D structure. The secondary structures of the ACD are indicated by B (beta-strands) or L (loops). The conserved amino acid sites (exact identity or similar physicochemical properties) are highlighted in gray. The amino acids at position 120 (in the human αB-crystallin sequence) are highlighted in red. The contact sites of these homologous residues (R107 in 1SHS, R108 in 1GME, and R158 in 2BOL ACD1) during the simulated annealing process are in green (see Table 3 for details); in the case of 1SHS, the main contacts (CI > 5) are indicated by white letters, and shown as 3D sticks in the Figure below. (B) 3D dimeric substructures of WT and mutants of the *M. jannaschii* Hsp16.5 during the simulated annealing process. From left to right: the dimer structures are shown in the upper line, with the 107 (R, K, D, G, or C) and E98 residues represented as sticks. Each 3D structure is partial, the main part of the N-terminal region being absent (until residue 33). These structures correspond to the 1SHS pdb dimer (chains A and C in dark and light black, respectively), and after simulated annealing, to the WT (blue), and the K (red), D (cyan), G (orange), and C (magenta) mutants. Each substructure displayed corresponds to one structure (of the 100 structures with the lowest potential energy) having the average rmsd (mean value or within the standard deviation). The lower line focuses on the local environment around the residue 107, its atoms being represented as spheres. The main intra and intermolecular contact sites observed during the simulated annealing process within the WT structure (white letters in the multiple sequence alignment above) are represented as green sticks: I37, S38, G39, G41, M43, L77, I79, and E98 (see Table 3 for details).

to obtain different pictures of the temperature induced changes. Because of its dynamic character and easy access, DLS was particularly convenient to measure R_h and % Pd in many conditions and therefore to analyze the temperature induced modifications and for fast trials. In addition, it was especially sensitive to the onset, with increasing temperature, of large size soluble aggregates. However, SAXS was particularly suited to obtain detailed information on the

Table 3: Contact Analysis: Sites and Conservation during the Simulated Annealing Processes[a]

			N-ter																	ACD					
										B1						*L12*				B2	B5				L57
R	1SHS	pdb								I37	S38			G39	K40	G41	F42	M43			L77		I79		E98*
		C.I.								8	11			10	4	14	1	6			14		19		7
	1GME	pdb							S32	A40	F41			A44						M46	L79	V80	V81		E100*
		C.I.							2	2	4			2						2	8	7	14		8
	2BOL	pdb			S59			N68								G95	E96				L137		V139		
		C.I.			6			1								1	11				4		20		
K	1SHS	pdb									S38			G39	K40	G41	F42	M43			L77		I79		E98*
		C.I.									8			8	13	15	4	9			11		20		6
	1GME	pdb	F10	D11						A40	F41	A42	N43	A44							L79		V81	S82	E100*
		C.I.	1	4						2	9	1	3	10							8		20	2	1
	2BOL	pdb			S59	E61	P62										E96				L137		V139		
		C.I.			5	7	1										7				2		14		
D	1SHS	pdb								I37	S38			G39	K40	G41	F42	M43	P44				I79		
		C.I.								4	3			13	7	9	5	15	1				2		
	1GME	pdb								A40	F41	A42	N43	A44							L79		V81		
		C.I.								1	2	13	19	19							8		20		
	2BOL	pdb			S59	E61															L137		V139	R140	
		C.I.			9	1															1		20	5	
G	1SHS	pdb																			L77		I79		
		C.I.																			16		20		
	1GME	pdb																			L79	V80	V81	S82	
		C.I.																			13	1	20	2	
	2BOL	pdb																			L137		V139	R140	
		C.I.																			3		20	3	
C	1SHS	pdb									S38			G39							L77	E78	I79		
		C.I.									1			1							8	1	20		
	1GME	pdb																			L79		V81		
		C.I.																			8		20		
	2BOL	pdb																			L137		V139		
		C.I.																			5		19		

[a] Summary of the contact sites (by hydrogen-bonding) of the equivalent hαB residue 120 (R for wild-type; K, D, G, and C for mutants) during the simulated annealing processes for *Methanococcus jannaschii* HSP16.5 (pdb code 1SHS), *Triticum aestivum* HSP16.9 (1GME), and *Taenia saginata* Tsp36 (2BOL). For each protein, these H-bonds were computed by the program Contact (CCP4), on the 20 structures with the lowest potential energy. The amino acids are indicated by a one-letter code and a number, which refers to the pdb numbering. * indicates an intermolecular contact site. A conservative index (C.I.) was computed for each contact site, as the number of structures (among the 20) where the given H-bond was observed. Table columns refer to homologous sites in the multiple sequence alignment (Figure 6A). The B1 beta-strand and the L12 loop (in italic) only refer to the *M. jannaschii* HSP16.5 (1SHS): the residues I37, S38, G39, and K40 are located in the beta-strand B1; instead, the residues G41, F42, M43, and P44 are located in the loop L12.

average quaternary structure. More importantly, SAXS allowed us to also study the pressure induced transitions (*31*). Pressure was demonstrated to yield assemblies with larger size and MW, similar to those observed when increasing temperature. The pressure induced transitions were mostly reversible, in contrast to the temperature induced transitions. The latter property was exploited to use SEC-MALS to follow the temperature induced MW changes.

The major experimental result obtained at that point was that each mutant behaved in its own way, yet the data consistently demonstrated that all of the R120 mutants, which formed larger and more polydisperse assemblies, exhibited lower stability than the hαB-WT. The mutants also presented structural transitions under stress, i.e., a size increase as a function of increasing temperature or pressure, indicative of structural disorganization (*31*). The transitions were, however, of lesser amplitude for the mutants than for the hαB-WT. Since it had been already shown that quaternary structure integrity was necessary for full chaperone-like activity (*36*), it was proposed that both the reduced chaperone-like activity and the modified transitions of the mutants were associated to perturbations in subunit exchange. Subunit exchange is most often tested with FRET experiments (*33, 49, 50*) and sometimes by IEF gel electrophoresis (*12, 51*) or mass spectrometry (*52, 53*). In the present study, we choose to design a subunit exchange assay based on anion exchange chromatography that was able to work in concentration conditions close to those used in DLS and SAXS experiments (of the order of 1 mg/mL) and did not require any probe. The only requirement was that the two initial particle populations had different isoelectric points (pI). The formation of new complexes, with intermediate pI, could then be easily demonstrated and resolved from the original ones. The assay was fast, of low cost, and reasonably demanding in terms of quantities. The charge difference between bαN and hαB was found to be sufficient to obtain a good resolution. The surprise was that the R120 mutant particles, less well organized than the hαB-WT, exchanged subunits faster. Relationships between the α-crystallin assembly state, chaperone-like activity, and subunit exchange had been documented in recent years (*24, 26, 33*). The results presented here demonstrated that all of the R120 mutants were able to associate an impaired chaperone activity and an enhanced exchange capacity. This property is reminiscent of a low-stability β-hairpin cysteine at the domain-pairing interface of the βB2-crystallin, which was proposed to favor a subunit exchange mechanism allowing the βB2-crystallin to interact with other β-crystallins (*54*).

In order to understand the structural origin of such a relationship, *in silico* methods were called for contribution. *In silico* site-directed mutagenesis was achieved, in the three 3D structures already known, at the R120 equivalent position, i.e., at R107 for HSP16.5, R108 for the HSP16.9, and R158 for Tsp36. In all three cases, four mutations were done, K D, G, and C. Then, MD simulations were carried out on isolated dimers in order to determine the consequences of the mutations on each substructure. One unambiguous result of the *in silico* approach was to show that any mutation at the R120 equivalent position modified the interaction between the residue at that position and its local environment (the L57 loop of the adjacent monomer in the case of HSP16.5 and HSP16.9). Only some of the intramonomer interactions in the B5 beta-strand were preserved in all cases. As a consequence, the L57 loop became less constrained and free to adopt a variety of conformations. Such a result suggested that monomer exchange could be facilitated as compared with dimer exchange, therefore increasing the overall subunit exchange capacity as observed in our experiments. A locally more flexible (or less constrained) structure would also be compatible with increased size and polydispersity. These results were reminiscent of the increased subunit exchange observed in the phosphorylation-mimicking mutation in αB (*55*). In that case, however, the chaperone-like activity was enhanced, whereas it was decreased for the αB-R120 mutants (*36*); this decreased chaperone-like activity would result from perturbations of the substrate interactive surface because of increased flexibility or decreased accessibility of the mutant structures.

Of course, one has to keep in mind that the simulated annealing processes were done on dimeric substructures and that the loss of contacts in the dimer could be compensated in the native assembly either by N-ter contacts or by other intersubunit contacts. Also, the L57 loop is highly variable from one species to the other. Whatever the limitations, the calculation suggested that any mutation at a position equivalent to the αB R120 position was able to induce a reduction of the initial inter- and intrasubunit contacts, not compensated by the formation of other contacts, and hence a destabilization of the whole structure. The calculation was also coherent with the experimental observations that the less severe consequences were observed for the K mutation and the more severe consequences being observed for the G mutation.

Eventually, the enhanced exchange capacity of the R120 mutants were in agreement with observations, that in environmental conditions close to those prevailing *in vivo*, the mutant particles could be at least partially rescued by the neighboring sHSPs, either constitutive or stress-induced (*56*). These exceptional properties point out once more the specific importance of the R120 residue, which, located at the edge of a substrate binding region, appears in addition as an essential node for a correct 3D folding, dynamic behavior, and functional antistress activity.

ACKNOWLEDGMENT

We gratefully acknowledge P. Vicart (University Paris 7) for constructive discussions, the European Synchrotron Radiation Facility (ESRF) for provision of the SAXS beamtime, and T. Narayanan for useful discussions and constant support at ID2 beamline.

REFERENCES

1. van Montfort, R., Slingsby, C., and Vierling, E. (2001) Structure and function of the small heat shock protein/α-crystallin family of molecular chaperones. *Adv. Protein Chem. 59*, 105–156.
2. Haslbeck, M., Franzmann, T., Weinfurtner, D., and Buchner, J. (2005) Some like it hot: The structure and function of small heat shock proteins. *Nat. Struct. Mol. Biol. 12*, 842–846.
3. Franck, E., Madsen, O., van Rheede, T., Richard, G., Huynen, M. A., and de Jong, W. W. (2004) Evolutionary Diversity of Vertebrate Small Heat Shock Proteins. *J. Mol. Evol. 59*, 792–805.
4. Bellyei, S., Szigeti, A., Pozsgai, E., Boronkai, A., Gomori, E., Hocsak, E., Farkas, R., Sumegi, B., and Gallyas, F. (2007) Preventing apoptotic cell death by a novel small heat shock protein. *Eur. J. Cell. Biol. 86*, 161–171.
5. Vicart, P., Caron, A., Guicheney, P., Li, Z., Prevost, M. C., Faure, A., Chateau, D., Chapon, F., Tome, F., Dupret, J. M., Paulin, D., and Fardeau, M. (1998) A missense mutation in the αB-crystallin chaperone gene causes a desmin-related myopathy. *Nat. Genet. 20*, 92–95.
6. Litt, M., Kramer, P., LaMorticella, D. M., Murphey, W., Lovrien, E. W., and Weleber, R. G. (1998) Autosomal dominant congenital cataract associated with a missense mutation in the human α-crystallin gene CRYAA. *Hum. Mol. Genet. 7*, 471–474.
7. Irobi, J., Van Impe, K., Seeman, P., Jordanova, A., Dierick, I., Verpoorten, N., Michalik, A., De Vriendt, E., Jacobs, A., Van Gerwen, V., Vennekens, K., Mazanec, R., Tournev, I., Hilton-Jones, D., Talbot, K., Kremensky, I., Van Den Bosch, L., Robberecht, W., Van Vandekerckhove, J., Broeckhoven, C., Gettemans, J., De Jonghe, P., and Timmerman, V. (2004) Hotspot residue in small heat-shock protein 22 causes distal motor neuropathy. *Nat. Genet. 36*, 597–601.
8. Evgrafov, O. V., Mersiyanova, I., Irobi, J., Van Den Bosch, L., Dierick, I., Leung, C. L., Schagina, O., Verpoorten, N., Van Impe, K., Fedotov, V., Dadali, E., Auer-Grumbach, M., Windpassinger, C., Wagner, K., Mitrovic, Z., Hilton-Jones, D., Talbot, K., Martin, J. J., Vasserman, N., Tverskaya, S., Polyakov, A., Liem, R. K., Gettemans, J., Robberecht, W., De Jonghe, P., and Timmerman, V. (2004) Mutant small heat-shock protein 27 causes axonal Charcot-Marie-Tooth disease and distal hereditary motor neuropathy. *Nat. Genet. 36*, 602–606.
9. Arrigo, A. P., Simon, S., Gibert, B., Kretz-Remy, C., Nivon, M., Czekalla, A., Guillet, D., Moulin, M., Diaz-Latoud, C., and Vicart, P. (2007) Hsp27 (HspB1) and alphaB-crystallin (HspB5) as therapeutic targets. *FEBS Lett. 581* (19), 3665–3674.
10. de Jong, W. W., Caspers, G. J., and Leunissen, J. A. (1998) Genealogy of the α-crystallin-small heat-shock protein superfamily. *Int. J. Biol. Macromol. 22*, 151–162.
11. Kim, K. K., Kim, R., and Kim, S. H. (1998) Crystal structure of a small heat-shock protein. *Nature 394*, 595–599.
12. van Montfort, R. L., Basha, E., Friedrich, K. L., Slingsby, C., and Vierling, E. (2001) Crystal structure and assembly of a eukaryotic small heat shock protein. *Nat. Struct. Biol. 8*, 1025–1030.
13. Stamler, R., Kappe, G., Boelens, W., and Slingsby, C. (2005) Wrapping the α-crystallin domain fold in a chaperone assembly. *J. Mol. Biol. 353*, 68–79.
14. Kennaway, C. K., Benesch, J. L., Gohlke, U., Wang, L., Robinson, C. V., Orlova, E. V., Saibil, H. R., and Keep, N. H. (2005) Dodecameric structure of the small heat shock protein Acr1 from Mycobacterium tuberculosis. *J. Biol. Chem. 280*, 33419–33425.
15. White, H. E., Orlova, E. V., Chen, S., Wang, L., Ignatiou, A., Gowen, B., Stromer, T., Franzmann, T. M., Haslbeck, M., Buchner, J., and Saibil, H. R. (2006) Multiple distinct assemblies reveal conformational flexibility in the small heat shock protein Hsp26. *Structure 14*, 1197–1204.
16. Shi, J., Koteiche, H. A., McHaourab, H. S., and Stewart, P. L. (2006) Cryoelectron microscopy and EPR analysis of engineered symmetric and polydisperse Hsp16.5 assemblies reveals determinants of polydispersity and substrate binding. *J. Biol. Chem. 281*, 40420–40428.
17. Haslbeck, M., Kastenmüller, A., Buchner, J., Weinkauf, S., and Braun, N. (2008) Structural dynamics of archaeal small heat shock proteins. *J. Mol. Biol. 378*, 362–374.

18. Aquilina, J. A., Benesch, J. L., Bateman, O. A., Slingsby, C., and Robinson, C. V. (2003) Polydispersity of a mammalian chaperone: Mass spectrometry reveals the population of oligomers in αB-crystallin. *Proc. Natl. Acad. Sci. U.S.A. 100*, 10611–10616.
19. Horwitz, J. (2003) α-crystallin. *Exp. Eye Res. 76*, 145–153.
20. Bloemendal, H., de Jong, W., Jaenicke, R., Lubsen, N. H., Slingsby, C., and Tardieu, A. (2004) Ageing and vision: Structure, stability and function of lens crystallins. *Prog. Biophys. Mol. Biol. 86*, 407–485.
21. Pasta, S. Y., Raman, B., Ramakrishna, T., and Rao, Ch. M. (2004) The IXI/V motif in the C-terminal extension of alpha-crystallins: alternative interactions and oligomeric assemblies. *Mol Vis. 10*, 655–662.
22. Pasta, S. Y., Raman, B., Ramakrishna, T., and Rao, Ch. M. (2003) Role of the conserved SRLFDQFFG region of α-crystallin, a small heat shock protein. Effect on oligomeric size, subunit exchange, and chaperone-like activity. *J. Biol. Chem. 278*, 51159–51166.
23. Ghosh, J. G., and Clark, J. I. (2005) Insights into the domains required for dimerization and assembly of human αB-crystallin. *Protein Sci. 14*, 684–695.
24. Sreelakshmi, Y., and Sharma, K. K. (2005) Recognition sequence 2 (residues 60−71) plays a role in oligomerization and exchange dynamics of αB-crystallin. *Biochemistry 44*, 12245–12252.
25. Aquilina, J. A., Benesch, J. L., Ding, L. L., Yaron, O., Horwitz, J., and Robinson, C. V. (2004) Phosphorylation of αB-crystallin alters chaperone function through loss of dimeric substructure. *J. Biol. Chem. 279*, 28675–28680.
26. Ghosh, J. G., Estrada, M. R., and Clark, J. I. (2005) Interactive domains for chaperone activity in the small heat shock protein, human αB-crystallin. *Biochemistry 44*, 14854–14869.
27. Ghosh, J. G., Jr, and Clark, J. I. (2006) N- and C-Terminal motifs in human αB-crystallin play an important role in the recognition, selection, and solubilization of substrates. *Biochemistry 45*, 13847–13854.
28. Santhoshkumar, P., and Sharma, K. K. (2006) Conserved F84 and P86 residues in alphaB-crystallin are essential to effectively prevent the aggregation of substrate proteins. *Protein Sci. 15*, 2488–2498.
29. Bhattacharyya, J., Padmanabha Udupa, E. G., Wang, J., and Sharma, K. K. (2006) Mini-alphaB-crystallin: a functional element of αB-crystallin with chaperone-like activity. *Biochemistry 45*, 3069–3076.
30. Haslbeck, M., Walke, S., Stromer, T., Ehrnsperger, M., White, H. E., Chen, S., Saibil, H. R., and Buchner, J. (1999) Hsp26: a temperature-regulated chaperone. *EMBO J. 18*, 6744–6751.
31. Skouri-Panet, F., Quevillon-Cheruel, S., Michiel, M., Tardieu, A., and Finet, S. (2006) sHSPs under temperature and pressure: The opposite behaviour of lens α-crystallins and yeast HSP26. *Biochim. Biophys. Acta 1764*, 372–383.
32. Franzmann, T. M., Menhorn, P., Walter, S., and Buchner, J. (2008) Activation of the Chaperone Hsp26 Is Controlled by the Rearrangement of Its Thermosensor Domain. *Mol. Cell 29*, 207–216.
33. Putilina, T., Skouri-Panet, F., Prat, K., Lubsen, N. H., and Tardieu, A. (2003) Subunit exchange demonstrates a differential chaperone activity of calf α-crystallin toward β_{LOW}- and individual γ-crystallins. *J. Biol. Chem. 278*, 13747–13756.
34. Bova, M. P., Yaron, O., Huang, Q., Ding, L., Haley, D. A., Stewart, P. L., and Horwitz, J. (1999) Mutation R120G in αB-crystallin, which is linked to a desmin-related myopathy, results in an irregular structure and defective chaperone-like function. *Proc. Natl. Acad. Sci. U.S.A. 96*, 6137–6142.
35. Treweek, T. M., Rekas, A., Lindner, R. A., Walker, M. J., Aquilina, J. A., Robinson, C. V., Horwitz, J., Perng, M. D., Quinlan, R. A., and Carver, J. A. (2005) R120G αB-crystallin promotes the unfolding of reduced α-lactalbumin and is inherently unstable. *FEBS J. 272*, 711–724.
36. Simon, S., Michiel, M., Skouri-Panet, F., Lechaire, J. P., Vicart, P., and Tardieu, A. (2007) Residue R120 is essential for the quaternary structure and functional integrity of human αB-crystallin. *Biochemistry 46*, 9605–9614.
37. Lomakin, A., Teplow, D. B., and Benedek, G. B. (2005) Quasielastic light scattering for protein assembly studies. *Methods Mol. Biol. 299*, 153–174.
38. Narayanan, T., Diat, O., and Boesecke, P. (2001) SAXS and USAXS on the high brilliance beamline at the ESRF. *Nucl. Instrum. Methods Phys. Res. A 467−468*, 1005–1009.
39. Boesecke, P. (2007) Reduction of two-dimensional small- and wide angle X-ray scattering data. *J. Appl. Crystallogr. 40*, S423–427.
40. Guinier, A., and Fournet, G. (1955) *Small Angle Scattering of X-rays*, Wiley, New York.
41. Edgar, R. C. (2004) MUSCLE: multiple sequence alignment with high accuracy and high throughput. *Nucleic Acids Res. 32* (5), 1792–1797.
42. Bennett-Lovsey, R. M., Herbert, A. D., Sternberg, M. J. E., and Kelley, L. A. (2008) Exploring the extremes of sequence/structure space with ensemble fold recognition in the program Phyre. *Proteins 703*, 611–625.
43. McLachlan, A. D. (1982) Rapid comparison of protein structures. *Acta Crystallogr., Sect. A 38*, 871–873.
44. Lindahl, E., Hess, B., and van der Spoel, D. (2001) GROMACS 3.0: A package for molecular simulation and trajectory analysis. *J. Mol. Model. 7*, 306–317.
45. Collaborative Computational Project, Number 4. (1994) The CCP4 suite: programs for protein crystallography. *Acta Crystallogr., Sect. D 50*, 760−763.
46. Kumar, L. V., Ramakrishna, T., and Rao, C. M. (1999) Structural and functional consequences of the mutation of a conserved arginine residue in αA and αB-crystallins. *J. Biol. Chem. 274*, 24137–24141.
47. Perng, M. D., Muchowski, P. J., van Den, I. P., Wu, G. J., Hutcheson, A. M., Clark, J. I., and Quinlan, R. A. (1999) The cardiomyopathy and lens cataract mutation in αB-crystallin alters its protein structure, chaperone activity, and interaction with intermediate filaments in vitro. *J. Biol. Chem. 274*, 33235–33243.
48. Simon, S., Fontaine, J. M., Martin, J. L., Sun, X., Hoppe, A. D., Welsh, M. J., Benndorf, R., and Vicart, P. (2007) Myopathy-associated alphaB-crystallin mutants: abnormal phosphorylation, intracellular location, and interactions with other small heat shock proteins. *J. Biol. Chem. 282*, 34276–34287.
49. Bova, M. P., Ding, L. L., Horwitz, J., and Fung, B. K. (1997) Subunit exchange of αA-crystallin. *J. Biol. Chem. 272*, 29511–29517.
50. Liang, J. J., and Liu, B. F. (2006) Fluorescence resonance energy transfer study of subunit exchange in human lens crystallins and congenital cataract crystallin mutants. *Protein Sci. 15*, 1619–1627.
51. Sun, T. X., and Liang, J. J. (1998) Intermolecular exchange and stabilization of recombinant human alphaA- and alphaB-crystallin. *J. Biol. Chem. 273*, 286–290.
52. Sobott, F., Benesch, J. L. P., Vierling, E., and Robinson, C. V. (2002) Subunit exchange of multimeric protein complexes. Real-time monitoring of subunit exchange between small heat shock proteins by using electrospray mass spectrometry. *J. Biol. Chem. 277* (41), 38921–38929.
53. Aquilina, J. A., Benesch, J. L., Ding, L. L., Yaron, O., Horwitz, J., and Robinson, C. V. (2005) Subunit exchange of polydisperse proteins: Mass spectrometry reveals consequences of αA-crystallin truncation. *J. Biol. Chem. 280*, 14485–14491.
54. MacDonald, J. T., Purkiss, A. G., Smith, M. A., Evans, P., Goodfellow, J. M., and Slingsby, C. (2005) Unfolding crystallins: The destabilizing role of a β-hairpin cysteine in βB2-crystallin by simulation and experiment. *Protein Sci. 14*, 1282–1293.
55. Ahmad, M. F., Raman, B., Ramakrishna, T., and Rao, Ch. M. (2008) Effect of phosphorylation on alpha B-crystallin: differences in stability, subunit exchange and chaperone activity of homo and mixed oligomers of αB-crystallin and its phosphorylation-mimicking mutant. *J. Mol. Biol. 375*, 1040–1051.
56. Ito, H., Kamei, K., Iwamoto, I., Inaguma, Y., Tsuzuki, M., Kishikawa, M., Shimada, A., Hosokawa, M., and Kato, K. (2003) Hsp27 suppresses the formation of inclusion bodies induced by expression of R120G αB-crystallin, a cause of desmin-related myopathy. *Cell. Mol. Life Sci. 60*, 1217–1223.

BI8014967